

Lattice discrete particle modeling of compressive failure in hollow concrete blocks

Fatemeh Javidan, Sharif Shahbeyk* and Mohammad Safarnejad

Faculty of Civil and Environmental Engineering, Tarbiat Modares University, Jalal Ale Ahmad Highway, P.O. Box 14115-143, Tehran, Iran

(Received March 25, 2013, Revised December 14, 2013, Accepted February 25 2014)

Abstract. This work incorporates newly introduced Lattice Discrete Particle Model (LDPM) to assess the failure mechanism and strength of hollow concrete blocks. Alongside, a method for the graphical representation of cracked surfaces in the LDPM is outlined. A slightly modified calibration procedure is also suggested and used to estimate required model parameters for a tested concrete sample. Next, the model is verified for a compressively loaded hollow block made of the very same concrete. Finally, four geometries commonly used in the production of hollow concrete blocks are selected, numerically simulated, and their failure properties are explored under concentric and eccentric compressions.

Keywords: concrete block; failure; lattice discrete particle model; graphical representation; calibration

1. Introduction

Due to their light weight, usability, as well as reasonable compressive performance, hollow concrete blocks are widely used in masonry structures. The blocks are considered the main building elements of such systems, where their geometrical design and mechanical properties predominantly decide the global behavior of block-works. Accordingly, various experimental and numerical researches have been conducted so far to identify the structural properties of hollow concrete blocks and link them with those of block-works (Maurenbrecher 1985, Maurenbrecher 1986, Barbosa and Hanai 2009). Furthermore, comprehensive studies can be found in which the effect of mortar and its bond to blocks are also investigated (Ramamurthy *et al.* 2000 and Andolfato *et al.* 2007). From loading point of view, hollow masonry works have been subjected to different states such as concentric and eccentric compression (Page and Shrive 1990 and Yi and Shrive 2003), flexure (Grimm and Tucker 1985), and shear (Drysedale *et al.* 2005).

With the significant advances of computational tools and procedures in past decades, the numerical simulation of hollow concrete blocks, as well as their assemblages (e.g. prisms, panels, or even walls), has been gained lots of interest among researchers. Three-dimensional elastic finite element analyses were conducted on both face-shell and fully-bedded mortared prisms under axial compression in Hamid and Chukwunenye (1986) to obtain detailed stress distributions in pre-cracking stage. The effects of mortar bedding, block geometry, number of joints, and stiffness of

*Corresponding author, Ph. D., E-mail: shahbeyk@modares.ac.ir

bearing plates were also investigated. Finally, recommendations for the determination of masonry compressive strength and evaluation of code provisions for testing of concrete masonry prisms were proposed. Similar investigations were conducted in Ganesan and Ramamurthy (1992) for concrete hollow-block masonry prisms.

To our best of knowledge, the first nonlinear finite element modeling of hollow masonry was appeared in Sayed-Ahmed and Shrive (1996). They considered compressive failure of constituent materials as well as their tensile cracking and tracked the behavior of face-shell-bedded hollow masonry since the appearance of web cracks up to almost final failure. A Drucker-Prager type plasticity model equipped with isotropic damage is used in Köksal *et al.* (2005) and the results of hollow block and grouted concrete block prisms were presented. Good agreements between experimental and numerical results were reported. The compressive strength correlation between the individual block, prism and basic wall panels for a new type of interlocking hollow mortar-less blocks (Thanoon *et al.* 2004) was the focus of a study by Jaafar *et al.* (2006). The same group extended their numerical part of studies by developing an incremental-iterative nonlinear finite element code where they accounted for the mechanical characteristics of interlocking dry joints, interaction between block units, progressive debonding between block and grout, and material nonlinearity (Thanoon *et al.* 2008 (a), (b)). The reliability of code was proven by demonstrating the nonlinear structural response and failure mechanism of individual block for both ungrouted and grouted interlocking systems which compared well with experimental results.

A simple homogenization technique and damage mechanics model were employed in Wu and Hao (2008) to obtain the equivalent elastic properties, strength envelope, and failure properties of a hollow concrete block masonry cell. The basic cell consisting of mortar and concrete components was modeled using a double scalar (corresponding to uniaxial tension and uniaxial compression) damage model and loaded in different displacement paths from which equivalent cell properties were derived. The accuracy of using these equivalent values was demonstrated for a hollow concrete masonry panel subjected to air blast loading.

The results of combined experimental testing and numerical simulation on axially loaded prisms with four different sets of block/mortar properties were reported in Barbosa *et al.* (2010). They showed that their three-dimensional finite element modeling based on plasticity and smeared cracking can satisfactorily predict the peak load and the failure modes. Del Coz Díaz *et al.* (2011), employed nonlinear finite element method and tried to optimize the design of hollow concrete blocks from both handling and structural points of view. Lu *et al.* (2011) also used nonlinear FE analysis and studied the effect of blocks cavity depth on the strength of slender unreinforced masonry hollow walls under eccentric vertical loads.

As outlined above, a wide range of numerical works on this type of structural elements, available in literature, are continuum based in which some do as well take advantage of tools such as plasticity, damage or crack models. These models are not considered perfect tools for predicting discontinuous behavior of materials, such as fracture, fragmentation, and damage localization. Moreover, as reported by Lourenco *et al.* (2006), continuum numerical models might significantly overestimate the compressive strength of masonry. To resolve the problem, Pina-Henriques *et al.* (2006) suggested a modified approach in which separate particles connected with interface elements were used in simulations.

The present work incorporates the newly introduced 3D lattice discrete particle model (Cusatis *et al.* 2003, Mencarelli, A. 2007, Cusatis *et al.* 2011(a)) for mesoscopic simulation of concrete and studies the failure mechanism and strength of hollow concrete blocks. The unique properties of LDPM in capturing different aspects of concrete complex behavior have been proven elsewhere

(see e.g. Alnaggar and Cusatis 2012, Alnaggar *et al.* 2013, Cusatis *et al.* 2011b, Schauffert and Cusatis 2012, Schauffert *et al.* 2012 and Smith *et al.* 2012). A systematic procedure for the graphical representation of cracks in LDPM is presented. Using a consistent calibration procedure, required model parameters are extracted for a concrete sample whose uniaxial compressive and tensile properties are available. The model is then verified for a concentrically tested hollow concrete block made of the very same concrete. Next, four types of commonly used hollow concrete blocks are selected and examined under concentric and eccentric compression. Finally, the effects of loading condition and block type on the failure properties of samples are discussed.

2. Lattice discrete particle model (LDPM)

Borrowing the ideas originally developed in the microplane constitutive modeling of materials, Cusatis *et al.* (2003) introduced a new approach for mesoscale simulation of concrete and named it Confinement Shear Lattice Model (CSLM). The CSLM discretizes concrete into a set of connected rigid cells each of which contains an aggregate and its surrounding mortar. The model generates spherical aggregates and packs them randomly within concrete sample. Then, a Delaunay tessellation whose vertices are the center points are used to create aggregate connectivity network. Finally, the geometrical data of this tessellation helps form a Voronoi-like structure which itself defines CSLM cells.

For future use, we first need to define the following terms (see Fig. 1).

- A connection between two neighboring cells is called a *strut*.
- The *mid-point* (**MidP**) of a strut is a point located at the mid-length of its counterpart belonging to the mortar.
- For each triangle whose edges are the struts, a *tri-point* (**TriP**) is defined as the center of the area obtained by subtracting from the area of that triangle the counterparts of the aggregate areas associated with that triangle.
- For each tetrahedron whose edges are the struts, a *tet-point* (**TetP**) is defined as the mass center of the volume obtained by subtracting from the volume of that tetrahedron the counterparts of the aggregate volumes associated with that tetrahedron.
- The area center of a triangle whose vertices are a MidP, a **TriP**, and a TetP, is called a *center-point* (**CenP**).
- Defining a plane perpendicular to a strut and passing its MidP, the *projected* tri-point (**PTriP**), tet-point (**PTetP**), and center point (**PCenP**) are defined as the projections of the corresponding TriP, TetP, and CenP on this plane.

Now, one can construct a set of triangles whose vertices are MidPs, PTriPs, and PTetPs. The assembly of such triangles defines the interface between neighboring particles.

The preliminary version of CSLM assumes that the interacting forces between two connected aggregates can be computed by determining the displacement jump vector at their MidP. In other words, the computational points (CPs) of CSLM are MidPs. Cusatis *et al.* (2003) assumes that the displacement jump at a CP, $\llbracket \mathbf{u}_{CP} \rrbracket$, is equal to

$$\llbracket \mathbf{u}_{CP} \rrbracket = \mathbf{u}(\mathbf{x}_{CP}^+) - \mathbf{u}(\mathbf{x}_{CP}^-) = \mathbf{A}_2(\mathbf{x}_{CP})\mathbf{Q}_2 - \mathbf{A}_1(\mathbf{x}_{CP})\mathbf{Q}_1 \quad (1)$$

where

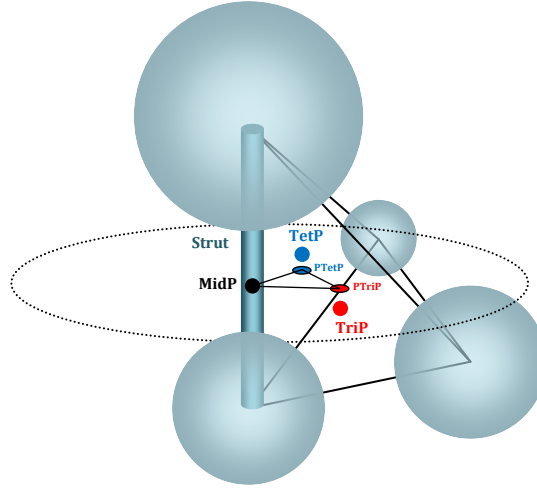


Fig. 1 Important geometrical features of an aggregates interface

$$\mathbf{A}_i(\mathbf{x}) = \begin{bmatrix} 1 & 0 & 0 & 0 & z - z_i & y_i - y \\ 0 & 1 & 0 & z_i - z & 0 & x - x_i \\ 0 & 0 & 1 & y - y_i & x_i - x & 0 \end{bmatrix} \quad (2)$$

$$\mathbf{Q}_i = [\mathbf{u}_i^T \quad \boldsymbol{\theta}_i^T]^T, \quad \mathbf{u} = [u_x \quad u_y \quad u_z]^T, \quad \boldsymbol{\theta} = [\theta_x \quad \theta_y \quad \theta_z]^T, \quad \mathbf{x} = [x \quad y \quad z]^T \quad (3)$$

\mathbf{u} , $\boldsymbol{\theta}$, and \mathbf{x} are the translational and rotational degrees of freedom at the center of an aggregate and its spatial coordinates, respectively. Index i distinguishes between two end aggregates of the strut. Using this calculated displacement jump, the following normal, ϵ_N , and tangential, ϵ_L and ϵ_M , strains are defined in Cusatis *et al.* (2003).

$$\epsilon_N = \mathbf{n}^T [\mathbf{u}_{\text{CP}}] / l = \mathbf{B}_{N2} \mathbf{Q}_2 - \mathbf{B}_{N1} \mathbf{Q}_1 \quad (4)$$

$$\epsilon_L = \mathbf{l}^T [\mathbf{u}_{\text{CP}}] / l = \mathbf{B}_{L2} \mathbf{Q}_2 - \mathbf{B}_{L1} \mathbf{Q}_1 \quad (5)$$

$$\epsilon_M = \mathbf{m}^T [\mathbf{u}_{\text{CP}}] / l = \mathbf{B}_{M2} \mathbf{Q}_2 - \mathbf{B}_{M1} \mathbf{Q}_1 \quad (6)$$

$$\mathbf{B}_{Ni} = (1/l) \mathbf{n}^T \mathbf{A}_i(\mathbf{x}_{\text{CP}}), \quad \mathbf{B}_{Li} = (1/l) \mathbf{l}^T \mathbf{A}_i(\mathbf{x}_{\text{CP}}), \quad \mathbf{B}_{Mi} = (1/l) \mathbf{m}^T \mathbf{A}_i(\mathbf{x}_{\text{CP}}) \quad (7)$$

\mathbf{n} is the unit vector directed along the strut and \mathbf{l} and \mathbf{m} are two mutually perpendicular unit vectors in tangential plane. l is the length of the strut. Cusatis *et al.* 2003 combined these strains and introduced the following strain measures.

$$\epsilon = \sqrt{\epsilon_N^2 + \alpha(\epsilon_M^2 + \epsilon_L^2)} = \sqrt{\epsilon_N^2 + \alpha\epsilon_T^2} \quad (8)$$

$$\tan \omega = \frac{\epsilon_N}{\sqrt{\alpha} \epsilon_T} \quad (9)$$

ϵ and ω are called effective and coupling strains, respectively. ϵ_T is the total shear strain. α is a dimensionless material property used to control overall elastic Poisson's ratio. Cusatis *et al.* (2003) used the principle of virtual work and showed that

$$\sigma_N = \sigma \frac{\epsilon_N}{\epsilon}, \quad \sigma_M = \sigma \frac{\alpha \epsilon_M}{\epsilon}, \quad \sigma_L = \sigma \frac{\alpha \epsilon_L}{\epsilon}, \quad \sigma = \sqrt{\sigma_N^2 + \frac{(\sigma_M^2 + \sigma_L^2)}{\alpha}} = \sqrt{\sigma_N^2 + \frac{\sigma_T^2}{\alpha}} \quad (10)$$

Cusatis *et al.* (2003) based the constitutive relation of CSLM on the following elastic boundary.

$$\sigma_b(\epsilon, \omega) = \sigma_0(\omega) \exp \left\{ \frac{K(\omega)}{\sigma_0(\omega)} \left(\epsilon - \frac{\sigma_0(\omega)}{E} \right) \right\} \quad (11)$$

E is mesoscale elastic modulus and $K(\omega)$ defines hardening-softening rates for different loading paths. $\sigma_0(\omega)$ is the initial effective strength function and is defined as below (see Fig. 2)

$$\sigma_0(\omega) = \begin{cases} \sigma_{01}(\omega) & \omega \leq \omega_0 \\ \sigma_{02}(\omega) & \omega > \omega_0 \end{cases} \quad (12)$$

$$\sigma_{01}(\omega) = \frac{\sigma_c}{\sqrt{s^2 + \alpha c^2}} \quad (13)$$

$$\sigma_{02} = \frac{-(\sigma_t + \sigma_a)s + \sqrt{[(\sigma_t + \sigma_a)s]^2 + \left[\alpha \left(\frac{\epsilon}{\mu} \right)^2 - s^2 \right] (\sigma_t + 2\sigma_a)\sigma_t}}{\alpha (c/\mu)^2 - s^2} \quad (14)$$

where

$$s = \sin \omega, c = \cos \omega, \sigma_a = 0.5\sigma_t \left[\frac{\sigma_s^2}{\mu^2 \sigma_t^2} - 1 \right] \quad (15)$$

μ and σ_a are respectively, the slope and the intersection of the hyperbola, $\sigma_{02}(\omega)$, asymptote with the σ_N axis. σ_t , σ_c , and σ_s are mesoscale tensile, compressive, and shear strength, respectively. ω_0 corresponds to the intersection of $\sigma_{01}(\omega)$ and $\sigma_{02}(\omega)$ curves.

The form below is used in Cusatis *et al.* (2003) for $K(\omega)$ to control the evolution of boundary

$$K(\omega) = \begin{cases} K_c \left[1 - \left(\frac{\omega + \pi/2}{\omega_0 + \pi/2} \right)^{n_c} \right] & \omega \leq \omega_0 \\ -K_t \left[1 - \left(\frac{\omega - \pi/2}{\omega_0 - \pi/2} \right)^{n_t} \right] & \omega > \omega_0 \end{cases} \quad (16)$$

Parameters K_c and n_c control nonlinear compressive and low shear-high compressive responses and K_t and n_t govern the nonlinear tensile, shear-tensile, and high shear-low compressive behaviors at meso-level.

Cusatis *et al.* (2006) slightly modified the CSLM and re-presented it. The main modification they made to the model was the position of computational points as transferred to the CGs of the interfaces. Furthermore, they used formula below for n_t to ensure correct energy dissipation.

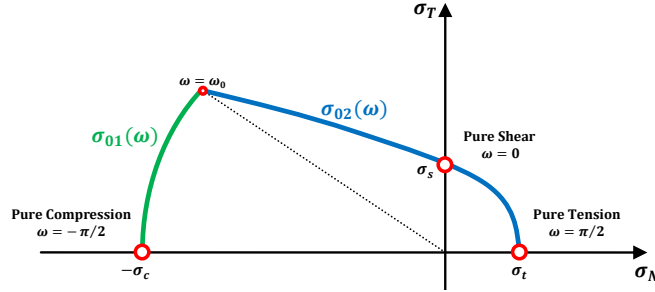


Fig. 2 Elastic boundary of the CSLM

$$n_t = \frac{\ln [K_t / (K_t - K_s)]}{\ln (1 - 2\omega_0 / \pi)} \quad (17)$$

where

$$K_t = \frac{2E}{l_t^{cr} / l - 1} \quad (18)$$

$$K_s = \frac{2\alpha E}{l_s^{cr} / l - 1} \quad (19)$$

Here $l_t^{cr} = 2E G_t / \sigma_t^2$ and $l_s^{cr} = 2\alpha E G_s / \sigma_s^2$ are the tensile and shear characteristic lengths of material, respectively. G_t is meso-level fracture energy for mode I and G_s is its counterpart for mode II.

In Mencarelli (2007), CSLM with its strut-based single-computational point interfaces was upgraded to LDPM which is equipped with facet-based multi-computational point cell-interfaces. To be more precise, the interacting forces between two neighboring aggregates are estimated in LDPM by first computing displacement jumps and strains at all their common PCenPs and then calculating corresponding stresses. This implies that, compared to its predecessor, the computational cost of LDPM is increased by one order, the cost paid to get rid of spurious (zero) deformation modes seen in original CSLM. The deteriorating effect of such spurious modes on final results of CSLM might best be seen as a null response of a cubic sample imposed to pure shear load.

The current study uses the very same constitutive model presented in Mencarelli (2007) unless a minor modification is made to the form of $K(\omega)$ for $\omega > \omega_0$ to ensure smooth transition of softening rate from K_t in pure tension to zero in pure shear and high shear-low compression states. To this end the previous function of $K(\omega)$ (Eq. (16)) has been substituted by the following simple formula

$$K(\omega) = \begin{cases} K_t \left(\frac{2\omega}{\pi} \right)^{n_t} & 0 < \omega \leq \frac{\pi}{2} \\ 0 & \omega_0 \leq \omega \leq \pi \end{cases} \quad (20)$$

Same formula is recently used in Mencarelli (2010). It needs to note that a new version of LDPM was introduced in Cusatis *et al.* (2011(a), (b)). Modifications were imposed on both the configuration of computational points and also re-formulations of mesoscopic constitutive relations in different loading states.

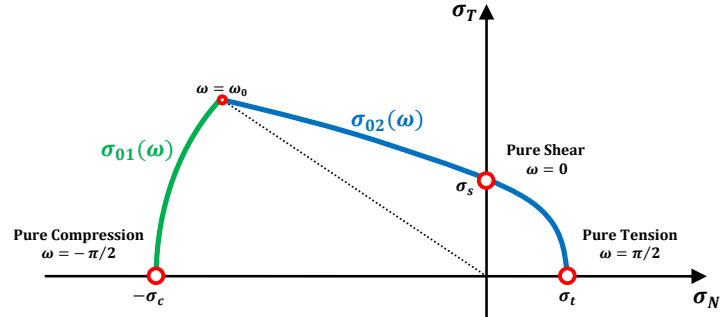


Fig. 2 Elastic boundary of the CSLM

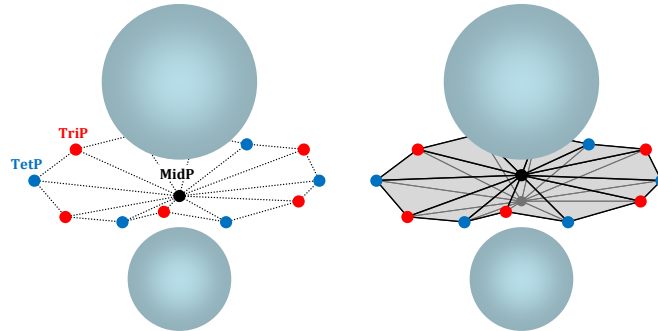


Fig. 3 Cracking at a typical MidP

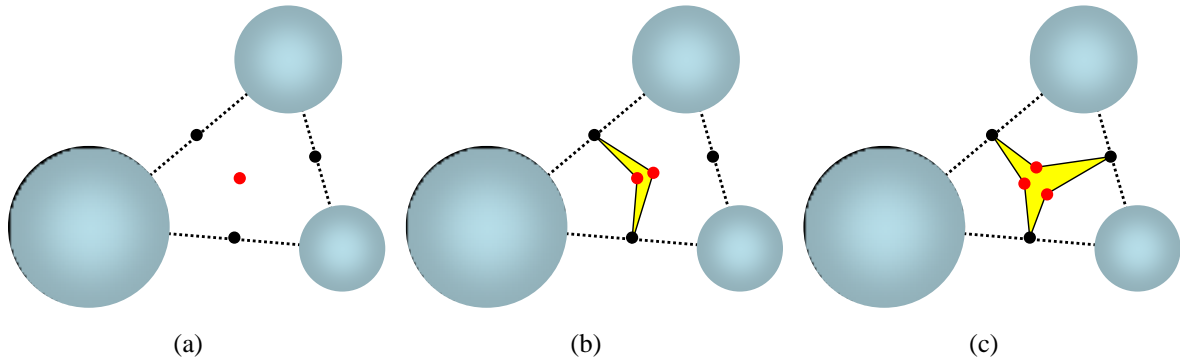


Fig. 4 Cracking patterns at a typical TriP (2D representation). (a) Uncracked, (b) Separation of one aggregate at TriP from other two aggregates, and (c) separation of three aggregates at TriP

3. Graphical representation

Lattice discrete particle model generates invaluable mesoscopic information such as axial and shear strains at computational points and interacting forces between neighboring aggregates, just to name a few. However, alongside these numerical values, it is essential to devise a method for realistic graphical representation of deformed configurations. This is extremely helpful in

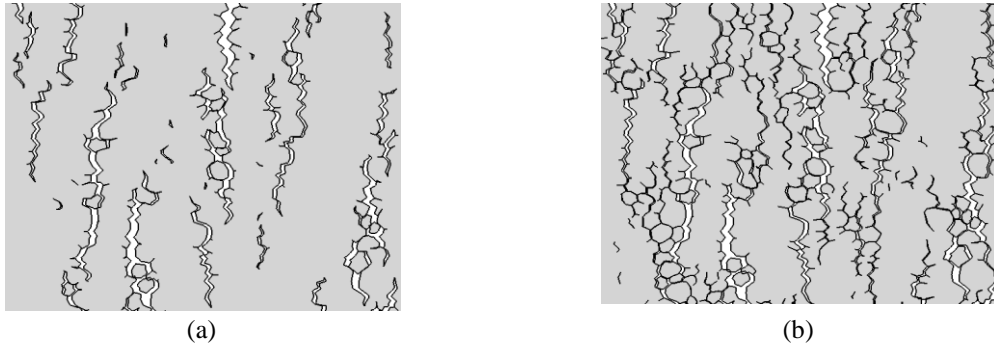


Fig. 5 Effect of strain threshold on graphical representation of cracks. (a) Critical effective strain=0.1 and (b) critical effective strain=0.01.

assessing the correctness of prepared models. Additionally, it helps create insight into main mechanisms underlying the failure of concrete samples. Concerning the nature of concrete and the structure of LDPM, the most interested phenomena to be traced might be the creation and propagation of cracks. Thus, in the first step, one needs to select a computable measure to decide which interacting facets should be shown cracked. This requirement can be readily fulfilled using the effective strain defined in Eq. (8). Being inherent in its definition, this parameter can differentiate between fractured and intact surfaces of mesostructure. The second step is to implement a consistent algorithm which adopts the values of effective strain at CPs and generates necessary geometrical data. In order to closely imitate cracked surfaces of real concrete specimens, the triangles whose vertices are the original and not projected mid-, tri-, and tet-points are used in graphical display. However, as mentioned before, all model variables are computed at PCenPs. In what follows the details of procedure employed in our home made graphical code are outlined.

- **Step 1:** A positive value is assumed for the critical effective strain, $\epsilon_{cr} > 0$.
- **Step 2:** All cell vertices are grouped according to their types.
- **Step 3:** The effective strain of a typical MidP, ϵ_{Strut} , is approximated as the average of effective strains at computational points associated with that strut. If condition $\epsilon_{Strut} > \epsilon_{cr}$ is met, triangles containing this MidP are separated as shown in Fig. 3, i.e. the original MidP is replaced with two new points whose coordinates are computed by adding the translocations $\mathbf{u}(\mathbf{x}_{CP}^+)$ and $\mathbf{u}(\mathbf{x}_{CP}^-)$ to its initial coordinates.
- **Step 4:** Three effective strains are computed at a typical TriP by averaging the effective strains of any two edges (struts) of the triangle enclosed the point. These three values are checked against the critical effective strain and then, as illustrated in Fig. 4, new cracked surfaces born according to the combination of criteria met.
- **Step 5:** Inspired by the previous step, four effective strains are computed at a TetP by averaging the effective strains of any three edges (struts) of the tetrahedron enclosed the point and again compared with ϵ_{cr} . Similar to TriPs, cracked surfaces are generated depending on the combination of criteria met.

Finally, it is worth to note that the smaller the magnitude of the critical effective strain, the more the number of cell facets shown cracked. As an example, Fig. 5 compares the graphical representations of a simple compressively 2D specimen loaded for two effective strain thresholds of 0.1 and 0.01.

4. Modeling, calibration, and verification

Referring to the descriptions provided in section 2, LDPM employs many different variables for the simulation of concrete. These variables can be broken down into two main categories; first, the input variables describing the geometrical characteristics, such as grain diameter, from which the model mixture is subsequently generated; and second, the mesoscale mechanical parameters which mainly govern the behavior of concrete. The calibration of mesoscopic parameters is not trivial and requires a systematic approach. The main idea behind an efficient calibration procedure is to understand how the mesoscale variables control the response of concrete at macroscale. To be more precise, based on what is expected from the behavior of a large scale standard concrete specimen under different loading conditions, one needs to obtain and introduce the related LDPM mesoscale mechanical properties of concrete to the model. This is exactly what has been chased by Mencarelli (2007). This study borrows the calibration steps of Mencarelli (2007) and combines them, whenever necessary, with useful analytical relations of CEB-FIP Model Code (1993) to propose the following slightly modified procedure.

1. The coefficient α is obtained from equation below

$$\alpha = \frac{1-4\nu}{1+\nu} \quad (21)$$

ν is the elastic Poisson's ratio. Note that the Poisson's ratio of normal concrete is in the range of 0.17-0.24. This equations has been borrowed from an earlier work on microplane modeling of concrete (see, Carol and Bazant 1997)

2. The normal Young's modulus of mesostructure, E_N , is determined from the elastic response of cylindrical sample under uniaxial compression by trial and error.

3. The mesoscopic compressive strength, σ_c , can be obtained from the result of hydrostatic compressive test. To be more precise, this parameter should be determined in such a way that failure initiation under pure hydrostatic pressure is accurately predicted. In the absence of such data, it is suggested to use the empirical curve of Fig. 6. In this figure and hereinafter, the normalized volumetric stress, σ_v^n , and strain, ϵ_v^n , are equal to

$$\sigma_v^n = \frac{\sigma_v}{f_c'} \quad (22)$$

$$\epsilon_v^n = \frac{\epsilon_v E}{f_c'} \quad (23)$$

where σ_v , ϵ_v , E , and f_c' are macroscopic volumetric stress, volumetric strain, elastic modulus, and compressive strength, respectively.

4. The initial compressive slope, K_c , is also calculated from hydrostatic compressive test. Note that this parameter decides the slope of volumetric stress-strain curve beyond the initial failure.

5. The mesoscopic tensile strength, σ_t , and the tensile fracture energy of mesostructure, G_t , need to be simultaneously determined from the tensile stress-strain response of concrete. In the absence of such data, one can use the following equations proposed by CEB-FIP Model Code (1993) to link the value of G_t to σ_t .

$$G_t = G_{t0} \left(\frac{f_{cm}}{f_{cm0}} \right)^{0.7} \quad (24)$$

where $f_{cm0} = 10$ MPa and G_{t0} is the base value of fracture energy which depends on the maximum aggregate size, d_{max} , as given in Table 1. f_{cm} is the compressive strength which can be estimated as

$$f_{cm} = f_{ck0} \left(\frac{f_{ctm}}{f_{ctk0,m}} \right)^{1.5} \quad (25)$$

Here, $f_{ctk0,m} = 1.4$ MPa and $f_{ck0} = 10$ MPa. f_{ctm} is the tensile strength.

6. The mesoscopic shear strength, σ_s and n_t , are simultaneously determined in a trial and error process in such a way that the strength and post-peak response of the concrete under uniaxial compression coincide with the experimental results.

7. The procedure outlined above indicates that, in order to effectively calibrate LDPM, at least tensile and unconfined compressive responses of concrete should be provided in advance. To comply with this requirement, and considering that the main focus of our study is the compressive strength of hollow concrete blocks, the experimental results of Barbosa (2004) and Barbosa and Hanai (2009) have been employed in our calibration and verification steps. Mechanical curves and specifications found from standard concrete tests in the aforementioned study are used. They tested

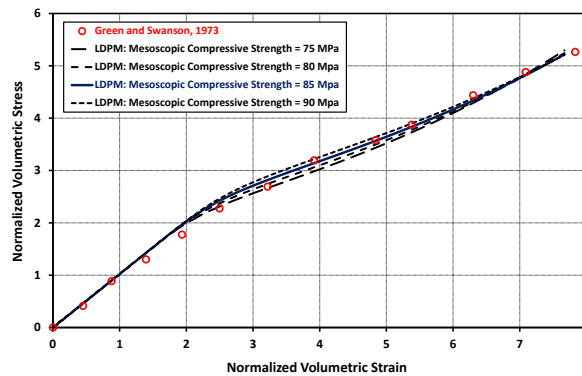


Fig. 6 The results of trial hydrostatic analyses to calibrate the parameter σ_c of the LDPM

Table 1 Base values of fracture energy, G_{t0} (CEB-FIP Model Code 1993).

d_{max} (mm)	G_{t0} (N.mm/mm ²)
8	0.025
16	0.030
32	0.058

Table 2 Calibrated values of the LDPM parameters.

LDPM Parameter	α	E_N (GPa)	σ_c (MPa)	K_c	σ_t (MPa)	n_t	σ_s (MPa)
Calibrated value	0.2	50	85	18	3.2	1.0	4.8

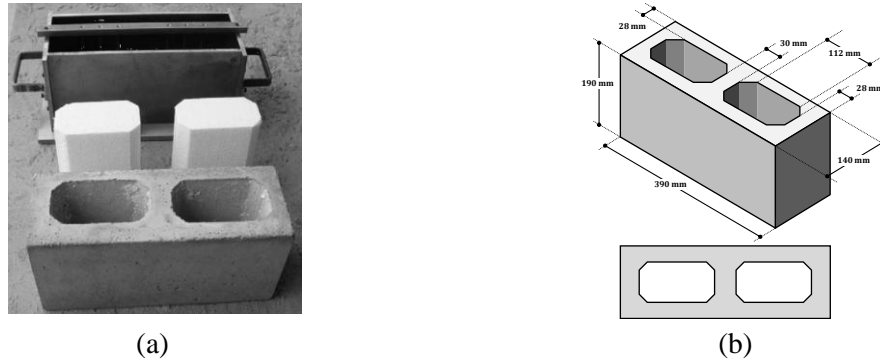


Fig. 7. The hollow concrete block tested in Barbosa and Hanai (2009). (a) Actual block and (b) its geometrical dimensions

Table 3 Numerically predicted and experimentally recorded properties of concrete.

	Elastic modulus (MPa)	Tensile strength (MPa)	Compressive strength (MPa)	Strain at peak compressive load
LDPM	19500	2.21	20.45	0.00270
experiment	19407	2.20	20.40	0.00271

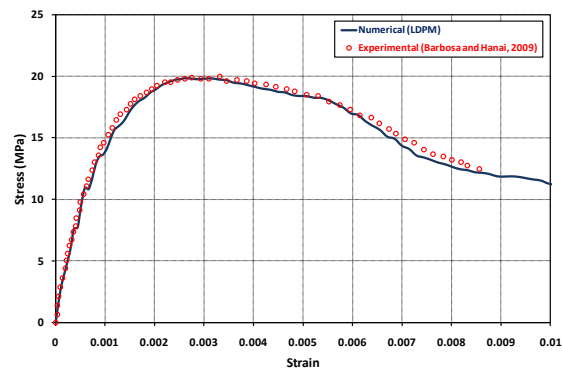


Fig. 8 Uniaxial compressive stress-strain curve of concrete

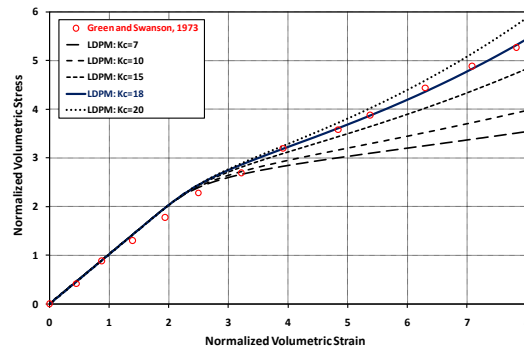


Fig. 9 The results of trial hydrostatic analyses to calibrate the parameter K_c of the LDPM

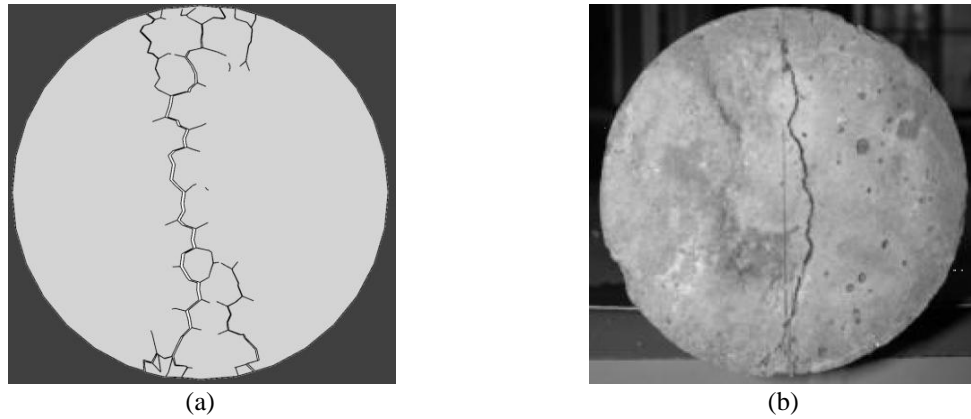


Fig. 10 Cracking pattern of concrete sample in indirect tensile test. (a) Numerical and (b) experimental

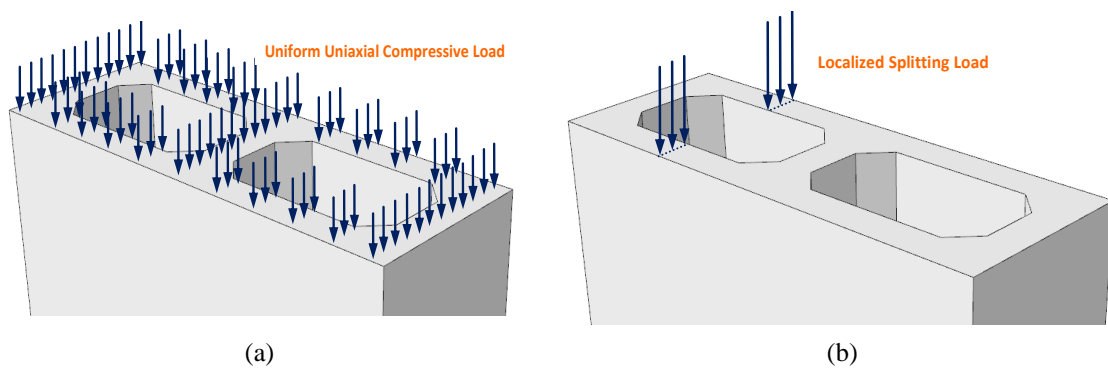


Fig. 11 Applied loads. (a) Uniform loading of uniaxial compression test and (b) localized loading of indirect tension test

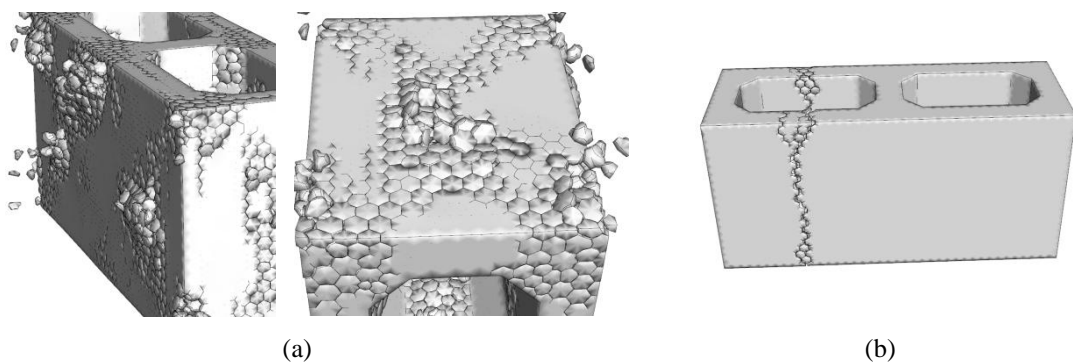


Fig. 12 Failure mechanism of the hollow block. (a) Uniaxial compression and (b) indirect tension

cylindrical samples of 100 mm in diameter and 200 mm in length under both uniaxial compression and tensile splitting (Brazilian indirect tension). Next, using similar concrete mixture, they produced the type of hollow blocks shown in Fig. 7 and examined them in compression and

indirect tension tests.

Fig. 8 presents the stress-strain curve of uniaxial compression test on cylindrical sample. Barbosa and Hanai (2009) did not provide the complete tensile stress-strain curve of the cylindrical sample and only reported tensile strength which is equal to 2.2 MPa. Moreover, as stated in Barbosa (2004), the Poisson's ratio and maximum aggregate diameter are 0.19 and 9.5 mm, respectively. In the absence of experimental data, the friction coefficient between loading plates and samples is assumed equal to 0.1.

Now, as outlined below, the proposed calibration procedure is followed step by step to obtain model parameters.

1. Putting $\nu = 0.19$ in Eq. 22, the coefficient α is approximately equal to 0.2.
2. A uniaxial compression test is simulated and, using a simple trial and error procedure, E_N is found equal to 50 GPa. As shown in Fig. 8, this value ensures good agreement between the initial elastic parts of experimental and numerical results.
3. A hydrostatic compression test is analyzed and its volumetric response is compared to the empirical curve of Fig. 6. Then, as shown in this figure, the value of σ_c is adjusted in such a way that failure initiation is correctly predicted.
4. In this step, using calibrated σ_c , the value of K_c is estimated by matching numerically predicted post-failure volumetric response to empirical curve of Fig. 9.
5. Considering $d_{max} = 9.5$ mm and using Eqs. 24 and 25, the tensile fracture energy of mesostructure is estimated as below

$$G_t = 16.25\sigma_t^{1.05} \quad (26)$$

Above equation is implemented in the code and several tensile splitting tests are simulated. Finally, for our concrete sample with splitting strength of 2.2 MPa, mesoscopic tensile strength is found equal to 3.2 MPa. Fig. 10a shows cracking pattern predicted by the model and compares it with that of actual sample (Fig. 10b).

6. Several trial uniaxial compressive tests are conducted from which the values of σ_s , and n_t are estimated equal to 4.8 MPa and 1.0, respectively. Fig. 8 depicts calculated stress-strain curve which compares well with experimental response.

Table 2 gathers LDPM calibrated parameters for this specific concrete and Table 3 compares empirically recorded and calculated tensile and compressive strengths. In addition, Fig. 8 depicts numerically predicted stress-strain curve and compares it with that of experiment. These results ensure the applicability of calibration procedure.

In the next step, the hollow concrete block tested by Barbosa and Hanai (2009) has been selected and simulated. As shown in Fig. 11, similar loading conditions (uniaxial compression and indirect tension) have been applied. Numerically calculated compressive and indirect tensile strengths are obtained equal to 20.4 MPa and 2.21 MPa, respectively. These values conform well to the experimental values of 20.2 MPa and 2.20 MPa. Moreover, Fig. 12 shows that, from failure mechanism point of view, the lattice discrete particle models of hollow concrete blocks satisfactorily predict experimental observations.

5. Concentric and eccentric compression of hollow concrete blocks

As the accuracy of numerical approach has been confirmed in section 4, this section focuses on

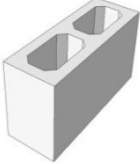
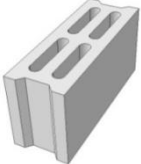
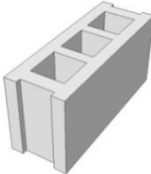
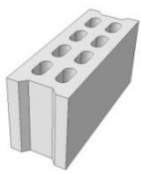
the failure of four different types of hollow concrete blocks containing 2, 3, 4, and 8 holes. The selected geometries are those commonly used in practice. The exterior dimensions of all blocks are 140 mm in width, 390 mm in length, and 190 mm in height. Table 4 presents the blocks and their net cross-section areas. Using calibrated parameters of section 4, blocks are simulated in LDPM. The number of computational points of prepared models is in the range of 0.5-1.0 million for each block.

As presented in Fig. 13, blocks are compressively loaded under ten eccentricities of 0, 20, 40, ..., 160, and 180 mm. The reason why eccentric loads are also studied in this paper is illustrated in Fig. 14. It shows a masonry wall under combined action of shear and compression. As seen, wherever interface mortar fails, interacting blocks begin to separate in tension dominated sides. This consequently causes eccentric compressive loading on blocks. The actual distribution of compressive load depends on the local field of displacements which itself is under the influence of various parameters such as the relative position of blocks in different layers and the mechanical properties of interface mortar.

Fig. 15 shows the stress-strain curves of analyzed hollow concrete blocks for different eccentricities. As predicted, in all cases examined, compressive strength decreases as eccentricity grows. The interesting point regarding ultimate strength is that, for the range of blocks studied in this paper, it is quite insensitive to the shape of block (see Fig. 16). Furthermore, almost linear dependency has been observed between ultimate strength and eccentricity.

Fig. 17 studies the results from dissipated energy density point of view. Dissipated energy density, defined as dissipated energy per unit volume, is a measure of ductility and shows the potential of a structural element to maintain its load bearing capacity. This figure shows that, for concentric loading condition, blocks with more holes are superior in terms of maintaining the rate of energy dissipation. The importance of this parameter is twofold. First, we can expect more energy dissipation capacity from block-works made of such units, and second, for constant deformations, residual load carrying capacity is bigger. The first item is a key characteristic of earthquake resistant structures, and the second one might be of great significance in preventing progressive collapse of structures under sever loads. Fig. 17 also shows that the importance of block shape fades as eccentricity grows.

Table 4 Simulated hollow concrete blocks

Block	Net area	Reference/producer	Shape	Block	Net area	Reference/Producer	Shape
1	$\approx 307 \text{ cm}^2$	2-Hole block (Barbosa 2004)		3	$\approx 372 \text{ cm}^2$	4-Hole block APCO (India)	
2	$\approx 289 \text{ cm}^2$	3-Hole block NIDCO (Spain)		4	$\approx 407 \text{ cm}^2$	8-Hole block APCO (India)	

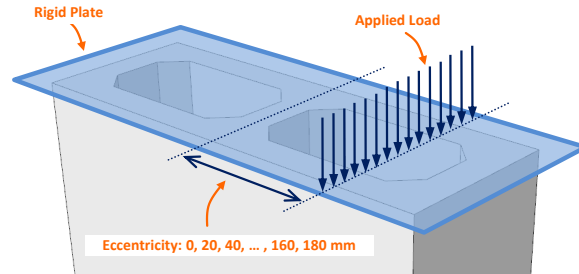


Fig. 13 Concentric and eccentric loading of hollow concrete blocks

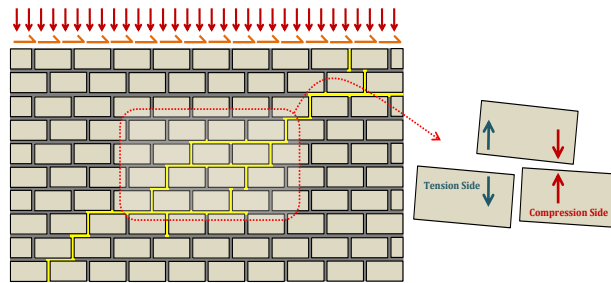


Fig. 14 Eccentric loading on hollow concrete blocks in a masonry wall under combined action of shear and compression

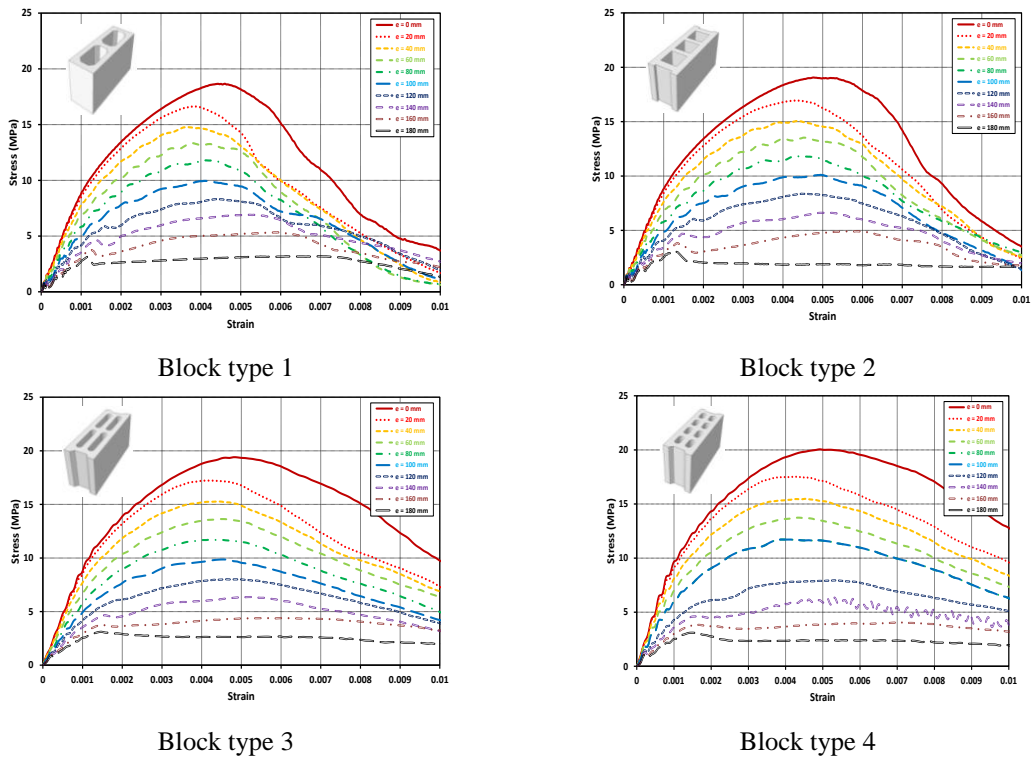


Fig. 15 Stress-strain curve of hollow concrete blocks under concentric and eccentric compression

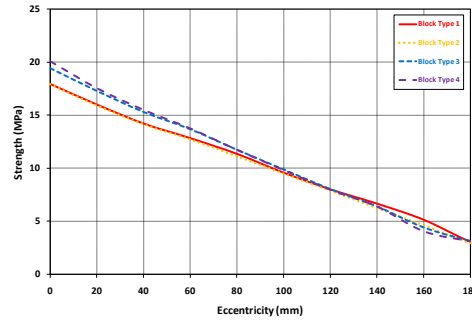


Fig. 16 Strength-eccentricity diagrams of analyzed samples

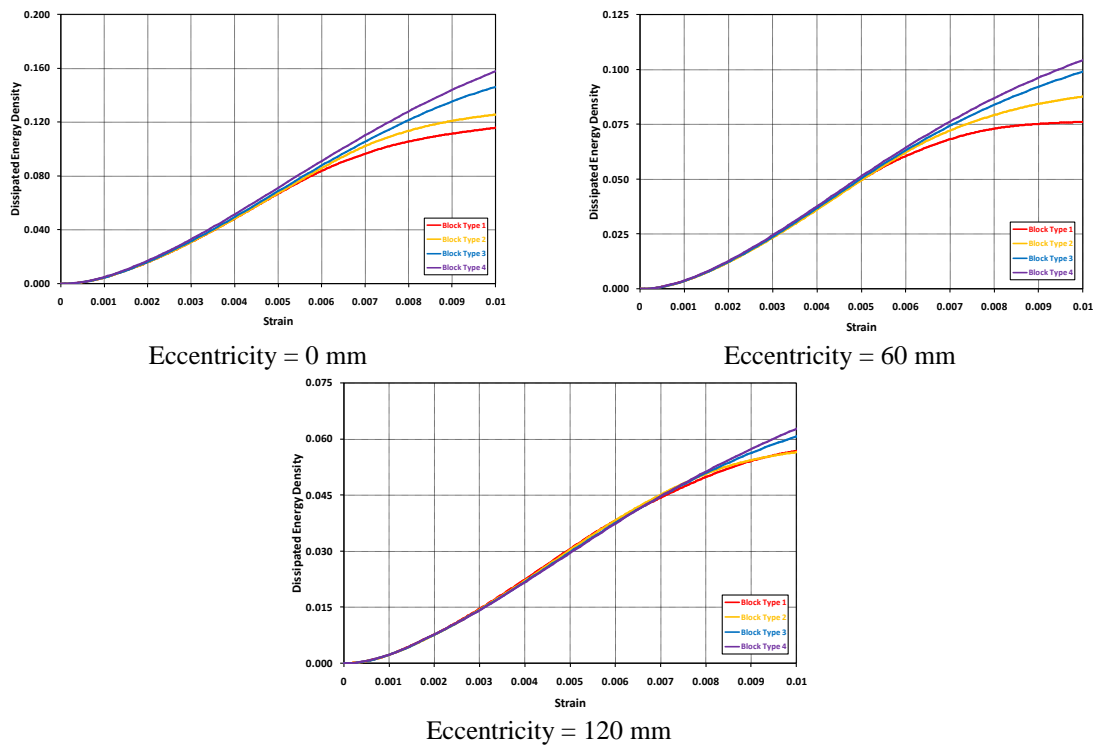


Fig. 17 Dissipated energy density versus strain

Fig. 18 presents the cracking patterns of four blocks analyzed at different eccentricities. Comparing the 4th block with the 3rd one, it is inferred that the existence of extra transversal walls is beneficial. In fact, the presence of extra longitudinal and transversal walls intensifies the confining state of stresses in the interior parts of blocks and thus increases the ductility of samples. This fact manifests itself with more complex fracturing and crushing patterns in the 3rd and 4th samples as shown in Fig. 18. In other words, comparing to the 1st and 2nd blocks, more diagonal cracks with bigger inclination angles are appeared in side walls (see cases in which $e = 0, 20$, or 80 mm).

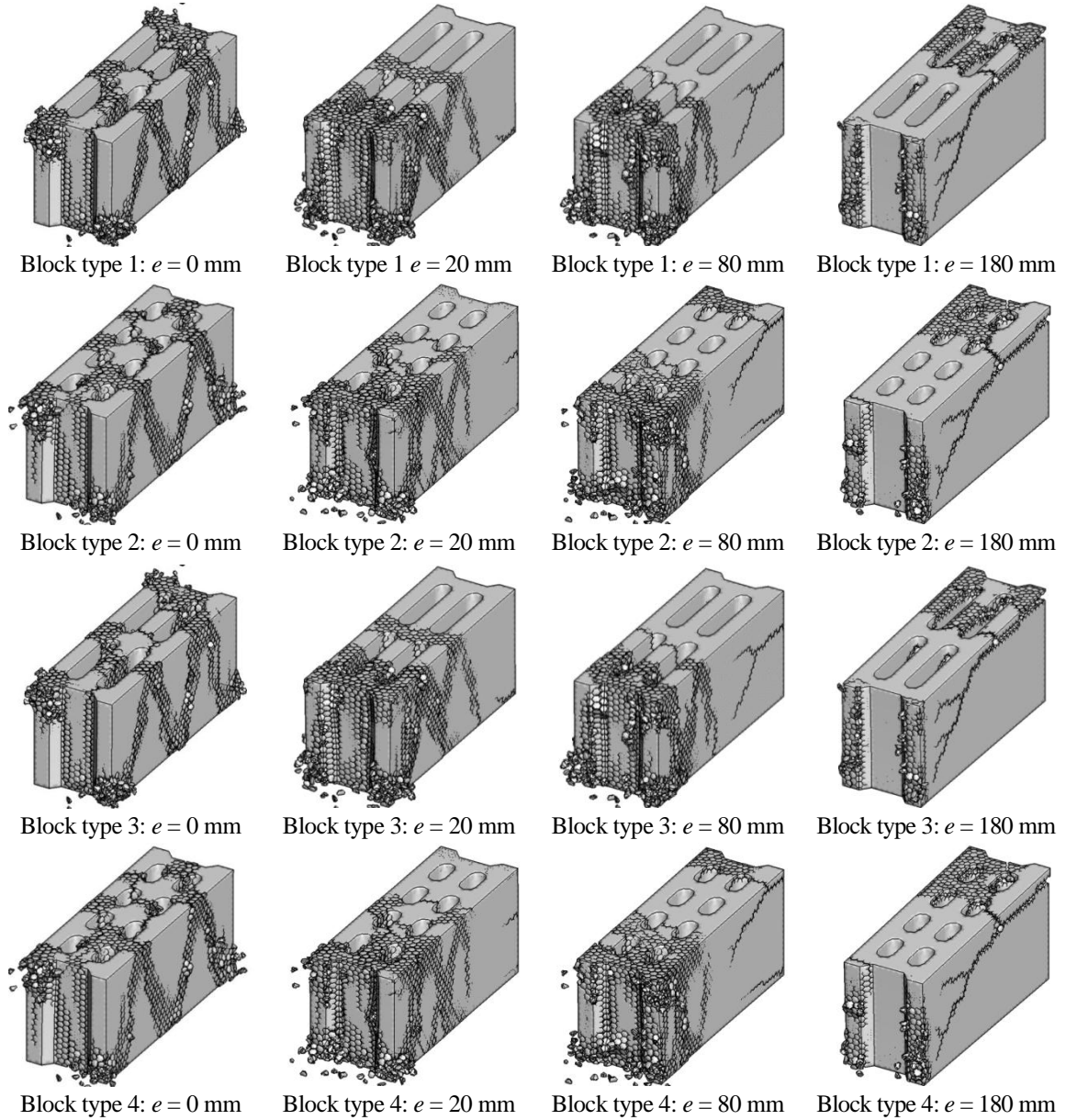


Fig. 18 Failure patterns of the hollow concrete blocks for different eccentricities

6. Conclusions

This work studies concentric and eccentric compressive failure of different hollow concrete blocks. To this end, the recently introduced lattice discrete particle model (LDPM) (Cusatis *et al.* 2003, Mencarelli 2007, Cusatis *et al.* 2011a) is incorporated and required computer codes are generated. The method can accurately accounts for different mesoscopic phenomena involved in the failure of concrete samples. Using simple formula proposed in CEB-FIP Model Code 1990

(1993) for the fracture energy of concrete, the calibration procedure suggested by Mencarelli (2007) has been refined and simplified. The model is then calibrated and verified against available experimental results of Barbosa (2004) and Barbosa and Hanai (2009). Alongside, a methodology for the graphical representation of LDPM outputs is thoroughly outlined.

In the second part, four types of commonly used hollow concrete blocks with 2, 3, 4, and 8 holes are considered and analyzed under different combinations of axial compression and flexure. The stress-strain curve and failure pattern are extracted for each sample. In the range of blocks studied, it is found that

- The ultimate strength-load eccentricity data of the simulated blocks are not sensitive to their shapes (maximum of 10 percent difference) and can be satisfactorily approximated by a line.
- Energy dissipation density curves show that, in contrary to insensitivity of ultimate strength to the shape of block, blocks with more (smaller) holes are beneficial in terms of dissipation capacity when compressed concentrically. This fact graphically manifests itself with more complex failure mechanisms in those samples. It needs to emphasis that this property is determining for structures experiencing earthquakes in which energy dissipation capacity of building blocks is of significant importance. It is also observed that this superiority fades as eccentricity grows.

References

- Alnaggar, M. and Cusatis, G. (2012), "Automatic parameter identification of discrete mesoscale models with application to the coarse-grained simulation of reinforced concrete structures", *20th Analysis and Computation Specialty Conference*, 406-417.
- Alnaggar, M., Cusatis, G. and Di Luzio, G. (2013), "Lattice discrete particle modeling (LDPM) of alkali-silica-reaction (ASR) deterioration of concrete structures", *Cem. Concr. Comp.*, **41**, 45-59.
- Andolfato, R.P., Camacho, J.S. and Ramalho, M.A. (2007), "Brazilian results on structural masonry concrete blocks", *ACI Mater. J.*, **104**(1), 33-39.
- Barbosa, C.S. (2004), "Resistencia e deformabilidade de blocos vazados de concreto e suas correlacoes com as propriedades mecanicas do material constituinte", M.Sc. Thesis, Universidade de Sao Paulo, Sao Paulo, Brazil.
- Barbosa, C.S. and Hanai, J.B. (2009), "Strength and deformability of hollow concrete blocks: correlation of block and cylindrical sample test results", *IBRACON Struct. Mater. J.*, **2**(1), 85-99.
- Barbosa, C.S., Lourenco, P.B. and Hanai, J.B. (2010), "On the compressive strength prediction for concrete masonry prisms", *Mater. Struct.*, **43**(3), 331-344.
- Carol, I. and Bazant, Z.P. (1997), "Damage and plasticity in microplane theory", *Int. J. Solids Struct.*, **34**(29), 3807-3835.
- CEB-FIP Model Code 1990 (1993), Comite Euro-International du Beton, Thomas Telford Services Ltd.
- Cusatis, G., Bazant, Z.P. and Cedolin, L. (2003), "Confinement-shear lattice model for concrete damage in tension and compression: I. Theory", *ASCE J. Eng. Mech.*, **129**(12), 1439-1448.
- Cusatis, G., Bazant, Z.P. and Cedolin, L. (2006), "Confinement-shear lattice CSL model for fracture propagation in concrete", *Comput. Meth. Appl. Mech. Eng.*, **195**(52), 7154-7171.
- Cusatis, G., Mencarelli, A., Pelessone, D. and Baylot, J.T. (2011a), "Lattice Discrete Particle Model (LDPM) for failure behavior of concrete. II: Calibration and validation", *Cem. Concr. Comp.*, **33**(9), 891-905.
- Cusatis, G., Pelessone, D. and Mencarelli, A. (2011b), "Lattice Discrete Particle Model (LDPM) for failure behavior of concrete. I: Theory", *Cem. Concr. Comp.*, **33**(9), 881-890.
- Del Coz Díaz, J.J., Nieto, P.J.G., Rabanal, F.P.A. and Martínez-Luengas, A.L. (2011), "Design and shape optimization of a new type of hollow concrete masonry block using the finite element method", *Eng.*

- Struct.*, **33**(1), 1-9.
- Drysdale, R.G., El-Dakhkhni, W.W. and Kolodziejski, E.A. (2005), "Shear capacity for flange-web intersection of concrete block shear walls", *ASCE J. Struct. Eng.*, **134**(6), 947-960.
- Ganesan, T. and Ramamurthy, K. (1992), "Behavior of concrete hollow-block masonry prisms under axial compression", *ASCE J. Struct. Eng.*, **118**(7), 1751-1762.
- Green, S.I. and Swanson, S.R. (1973), "Static constitutive relations for concrete", *Rep. No. AFWL-TR-72-2*, Air Force Weapons Lab., Kirtland Air Force Base, Albuquerque, NM, USA.
- Grimm, C.T. and Tucker, R.L. (1985), "Flexural strength of masonry prisms versus wall panels", *ASCE J. Struct. Eng.*, **111**(9), 2021-2032.
- Hamid, A.A. and Chukwunye, A.O. (1986), "Compression behavior of concrete masonry prisms", *ASCE J. Struct. Eng.*, **112**(3), 605-613.
- Jaafar, M.S., Thanoon, W.A., Najm, A.M.S., Abdulkadir, M.R. and Abang-Ali, A.A. (2006), "Strength correlation between individual block, prism and basic wall panel for load bearing interlocking mortarless hollow block masonry", *Constr. Build. Mater.*, **20**(7), 492-498.
- Köksal, H.O., Karakoç, C. and Yildirim, H. (2005), "Compression behavior and failure mechanisms of concrete masonry prisms", *ASCE J. Mater. Civil Eng.*, **17**(1), 107-115.
- Lourenço, P.B. and Pina-Henriques, J.L. (2006), "Validation of analytical and continuum numerical methods for estimating the compressive strength of masonry", *Comp. Struct.*, **84**(29-30), 1977-1989.
- Lu, M. and Schultz, A.E. (2011), "Influence of cavity dimension on the stability of eccentrically loaded slender unreinforced masonry hollow walls", *Constr. Build. Mater.*, **25**(12), 4444-4453.
- Maurenbrecher, A.H.P. (1985), "Axial compression tests on masonry walls and prisms", *Proceedings of the Third North American Masonry Conference*, Arlington, June.
- Maurenbrecher, A.H.P. (1986), "Compressive strength of hollow concrete blockwork", *Proceedings of the Fourth Canadian Masonry Symposium*, New Brunswick, Canada, June.
- Mencarelli, A. (2007), "The lattice discrete particle model (LDPM) for concrete: Calibration and validation under quasi-static loading conditions", M.Sc. Thesis, Rensselaer Polytechnic Institute, New York.
- Mencarelli, A. (2010), "Numerical simulation of the effect of blast and penetration on reinforced concrete structures", Ph.D. Dissertation, Rensselaer Polytechnic Institute, New York, USA.
- Page, A.W. and Shrive, N.G. (1990), "Concentrated loads on hollow concrete masonry", *ACI Struct. J.*, **87**(4), 436-444.
- Pina-Henriques, J.L. and Lourenço, P.B. (2006), "Masonry compression: A numerical investigation at the meso-level", *Eng. Comput.*, **23**(4), 382-407.
- Ramamurthy, K., Sathish, V. and Ambalavanan, R. (2000), "Compressive strength prediction of hollow concrete block masonry prisms", *ACI Struct. J.*, **97**(1), 61-67.
- Sayed-Ahmed, E.Y. and Shrive, N.G. (1996), "Nonlinear finite element model of hollow masonry", *ASCE J. Struct. Eng.*, **122**(6), 683-689.
- Schauffert, E., Cusatis, G., Pelessone, D., O'Daniel, J. and Baylot, J. (2012), "Lattice discrete particle model for fiber-reinforced concrete. II: Tensile fracture and multiaxial loading behavior", *ASCE J. Eng. Mech.*, **138**(7), 834-841.
- Schauffert, E.A. and Cusatis, G. (2012), "Lattice discrete particle model for fiber reinforced concrete (LDPM-F): I Theory", *ASCE J. Eng. Mech.*, **138**(7), 826-833.
- Smith, J., Cusatis, G., Pelessone, D., O'Daniel, J. and Baylot, J. (2012), "Calibration and validation of the lattice discrete particle model for ultra high- performance fiber-reinforced concrete", *20th Analysis and Computation Specialty Conference*, pp. 394-405.
- Thanoon, W.A., Alwathaf, A.H., Noorzaei, J., Jaafar, M.S. and Abdulkadir, M.R. (2008a), "Finite element analysis of interlocking mortarless hollow block masonry prism", *Comput. Struct.*, **86**(6), 520-528.
- Thanoon, W.A., Alwathaf, A.H., Noorzaei, J., Jaafar, M.S. and Abdulkadir, M.R. (2008b), "Nonlinear finite element analysis of grouted and ungrouted hollow interlocking mortarless block masonry system", *Eng. Struct.*, **30**(6), 1560-1572.
- Thanoon, W.A., Jaffar, M.S., Abdulkadir, M.R., Abang-Ali, A.A., Trikha, D.N. and Najm, A.M.S. (2004), "Development of an innovative interlocking load bearing hollow block system in Malaysia", *Constr.*

Build. Mater., **18**(6), 445-454.

Wu, C. and Hao, H. (2008), "Numerical derivation of averaged material properties of hollow concrete block masonry", *Eng. Struct.*, **30**(3), 870-883.

Yi, J. and Shrive, N.G. (2003), "Behaviour of partially grouted hollow concrete masonry subjected to concentrated loads", *Can. J. Civil Eng.*, **30**(1), 191-202.

CC